Influence of Tantalum composition on mechanical behavior and deformation mechanisms of $TiZrHfTa_x$ high entropy alloys

Yuhe Huang [a,b], Junheng Gao [a,c,*], Shuize Wang [c], Dikai Guan [a], Yidong Xu [a,d], Xiaogang Hu [b], W.Mark Rainforth [a], Qiang Zhu [b*], Iain Todd [a]

[a]Department of Materials Science and Engineering, University of Sheffield, Sheffield, S1 3JD, UK

[b]Department of Mechanical and Energy Engineering, Southern University of Science and Technology, Shenzhen, 518055, China

[c]Beijing Advanced Innovation Center for Materials Genome Engineering, University of Science and Technology Beijing, Beijing 100083, China

[d]Department of Orthopaedics, Shanghai Key Laboratory for Prevention and Treatment of Bone and Joint Diseases, Shanghai Institute of Traumatology and Orthopaedics, Ruijin Hospital, Shanghai Jiao Tong University School of Medicine, 197 Ruijin 2nd Road, Shanghai 200025, PR China.

Abstract

The effects of metastability engineering on tuning deformation behavior and deformation mechanisms in $TiZrHfTa_X$ (x=1.00, 0.80, 0.60, 0.50) refractory body centered cubic (BCC) high entropy alloys were investigated, with specific emphasis on elucidating the underlying interplay between phase stability, mechanical property, and deformation twins. It was found that in proper thermomechanical treated samples, a variation of tantalum content can effectively tune the activation of various deformation mechanisms. Detailed electron back-scattered diffraction and transmission electron microscopy analyses revealed for the first time that $\{332\}<11\bar{3}>_{BCC}$ twinning, deformation induced α'' phase, $\{111\}_{\alpha''}$ type I and $<\bar{2}11>_{\alpha''}$ type II twinning can be sequentially activated in $TiZrHfTa_X$ (x=1.00, 0.80, 0.60, 0.50) high entropy alloys with decreasing the content of tantalum. The comprehensive strengthening effect of transformation induced plasticity and twinning induced plasticity, was discussed and attributed as the pivotal factor for the improved work hardening capability and

mechanical performances, especially for alloys with lower tantalum contents. Consequently, we extended the conventional Bo-Md diagram that was originally developed for BCC titanium alloys for deformation mechanism evaluation to BCC high entropy alloys on the basis of current results, which sheds light on the design of ductile BCC high entropy alloys with expected deformation mechanisms and optimized mechanical performance.

Keywords

High-entropy alloys; Work hardening capability; Deformation induced twinning; Martensitic transformation; Bo-Md diagram.

1. Introduction

High entropy alloys have attracted substantial interests in the past decade due to their promising mechanical performance at both ambient and extreme environmental conditions. Exhibiting high thermal softening resistance and microstructural stability at elevated temperatures, refractory body centered cubic (BCC) high-entropy alloys, a subgroup of the complex concentrated alloy system which is mainly composed of group IVB and VB refractory elements, have aroused considerable attention[1]. Numerous high strength refractory BCC high entropy alloys have been developed so far, yet a great majority of them suffer poor ductility because of the lack of proper deformation mechanisms at ambient temperature, which hinders their practical applications[1–4].

Attempts to ductilize refractory BCC high entropy alloys have been conducted on refractory elements based four or five multi-components high entropy alloys through metastability engineering, from which the deformation mechanisms of BCC high entropy alloys can be tailored from dislocation slip to transformation induced plasticity (TRIP) by tuning the parent BCC phase stability[5,6]. The strengthening effects of martensitic phase transformation have been extensively studied and found that with varying BCC phase stabilities, stress/strain-induced hexagonal α[5–7], hexagonal α'[8–

10] and orthorhombic α''[11–13] phase transformation could be successfully activated in refractory BCC high entropy alloys. The resultant TRIP effects effectively alleviated the plastic instability in refractory BCC high entropy alloys, thus improving the uniform ductility by maintaining an appreciable work-hardening capability. Another feasible approach to enhance the mechanical behavior lies in introducing deformation induced twinning, as evidenced by the twinning induced plasticity (TWIP) effect in metastable face centered cubic (FCC) high entropy alloys[14–17]. However, in contrary to the widely studied TWIP effect in FCC high entropy alloys, deformation induced twins in refractory BCC high entropy alloys have not received much attention yet. Only in very recent attempts, based on the conventional Bo (the covalent bond strength between titanium and alloying elements) and Md (the mean d-orbital energy level) map originally proposed by Kuroda co-workers[18] and later by Abdel-Hady co-workers[19], a ductile titanium-rich Ti48.9Zr32.0Nb12.6Ta6.5 (at. %) medium entropy alloy (MEA) was developed with $\{112\}<11\bar{1}>_{BCC}$ twinning as dominant deformation mechanism[20]. The interaction between dislocations and deformation induced twinning was believed to play a crucial role in improving mechanical performance of this alloy. In addition, Wang co-workers[12] reported a titanium rich refractory Ti48Zr20Hf15Al10Nb7 (at. %) high entropy alloy, and found that, besides the stress induced α'' phase, a $\{111\}_{\alpha''}$ twinning was observed at 10% strained sample which was believed to be responsible for the continuous deformation of the alloy to a high stress and strain level. In addition, similar martensitic twinning was also captured in deformation induced α' phase of as-cast metastable TiZrHfTa BCC high entropy alloys[5].

Although deformation induced twinning in the parent BCC phase and deformation induced martensite phase have been observed in metastable refractory BCC high entropy alloys, the underlying activation mechanisms remain unclear. Referring to the conventional counterparts of the metastable refractory IVB elements based BCC high entropy alloys, e.g., BCC titanium alloys, deformation mechanisms, i.e., dislocation

slip, deformation induced twinning, deformation induced martensite, or a combination of any of these, show strong dependence upon the phase stability of the parent BCC phase[21,22]. Therefore, it is pertinent to deduce that the mechanical performance and the relevant deformation mechanisms of refractory BCC high entropy alloys should be also highly dependent on the chemical and structural stability of the parent BCC phase which could be efficiently tuned by the addition of BCC stabilizers such as vanadium, iron, molybdenum, and tantalum. Therefore, inspired by the potential to further improve the mechanical performance of refractory BCC high entropy alloys through introducing the comprehensive TWIP effect in addition to the TRIP effect, it is meaningful to investigate the effect of BCC stabilizers on tuning the deformation mechanisms and mechanical performance of refractory BCC high entropy alloys.

In the present work, the IVB group elements based $TiZrHfTa_x$ (x=1.00, 0.80, 0.60, 0.50) alloys with different amounts of tantalum, a strong BCC phase stabilizer, were selected to investigate the influence of BCC phase stability on the activation and cooperation among different deformation mechanisms, and thus the mechanical performance of the refractory BCC high entropy alloys. Proper thermomechanical treatment was performed on the selected compositions to ensure the chemical homogeneity and stability of the parent BCC phase at its original state. The underlying mechanisms responsible for the change of mechanical properties were carefully analysed with particular emphasis on the deformation induced twinning in the parent BCC and deformation induced martensite phase.

2. Materials and Methods

The nominal compositions of the alloys investigated in the current work are $TiZrHfTa_x$ (in molar ratio, x=1.00, 0.80, 0.60, 0.50, and denoted as Ta1, Ta0.8, Ta0.6 and Ta0.5 in following sections). The ingots of these alloys were prepared by arc melting the pure metals (purity above 99.9 wt.%) under a Titanium-gettered low-pressure high-purity argon atmosphere. Ingots were remelted at least five times for chemical homogeneity and subsequently cast into a water-cooled copper mold with

internal dimensions of 6 × 7 × 30 mm. Samples were further homogenized in vacuum sealed quartz tubes at 1373 K for 0.5 hour and subsequently quenched in water by breaking the tube simultaneously. Finally, after cold rolling with a reduction in thickness of ~85%, the samples were annealed in vacuum sealed quartz tubes at 1173 K for 0.5 hour and subsequently water quenched.

The flat dog-bone-shaped tensile samples were cut by electrical discharge machining from the annealed plates with a gauge length of 3× 12.5× 1 mm. Before testing, the samples were polished using P2000 grit SiC grinding paper to remove the possible oxidation layer at surface. Tensile tests were then performed on a ZWICK Z050TH testing system coupled with a laser extensometer at a nominal strain rate of 4×10^{-4} s^{-1} at ambient temperature. Tensile tests were performed along the rolling direction and at least 3 measurements were performed for each alloy. Phase identification was carried out by X-ray diffraction on Bruker D2 Phaser with a Copper-Kα (λ = 1.5406 Å) radiation source. The diffractograms were analyzed by the Rietveld refinement method using the TOPAS X-ray diffraction post-processing software. The microstructure analyses were carried out by a FEI Inspect F50 field emission gun scanning electron microscope fitted with an Oxford Instruments electron backscatter diffraction detector operating at 25 kV with a step size of 0.05-0.2 μm. Electron backscatter diffraction specimens were mechanically polished down to 3 μm diamond suspension and then ion polished with a Gatan PECS II ion polishing system under a condition of 3 kV, 5° for 15 minutes to remove possible contamination and residual deformation in the surficial layer that induced by mechanical polishing. The quantitative analysis of electron backscatter diffraction data was performed by HKL's CHANNEL5 electron backscatter diffraction post-processing software. Detailed microstructural characterizations were completed by FEI Talos F200X G2 transmission electron microscopy with an accelerating voltage of 200 kV. Transmission electron microscopy foils were prepared by twin-jet electropolishing (Struers TenuPol 5) with a solution of 5% perchloric acid, 35% 2-butoxyethanol and 60% methanol at 24 V and

243K. The foils were then put into a Gatan Precision Ion Polishing system (PIPS II) for final cleaning by ion polishing at 0.3 kV for 20 s.

3. Results and discussion

3.1. Phase constitution and mechanical performance

Representative X-ray diffraction patterns of $TiZrHfTa_x$ (x = 1.00, 0.80, 0.60, 0.50) after annealing at 1173 K for 0.5 hour are shown in Figure 1a, where a single BCC solid solution phase is observed for all the alloys. The relative content of titanium, zirconium and hafnium increases with a decrease of tantalum content from equimolar Ta1 to Ta0.5, which results in the BCC phase lattice parameter expansion from 3.445 Å (Ta1) to 3.448 Å (Ta0.8), 3.451 Å (Ta0.6) and 3.452 Å (Ta0.5). The lattice parameter expansion is attributed to the addition of tantalum whose atomic radius (1.47 Å) is close to titanium (1.46 Å) but smaller than zirconium (1.6 Å) and hafnium (1.59 Å).

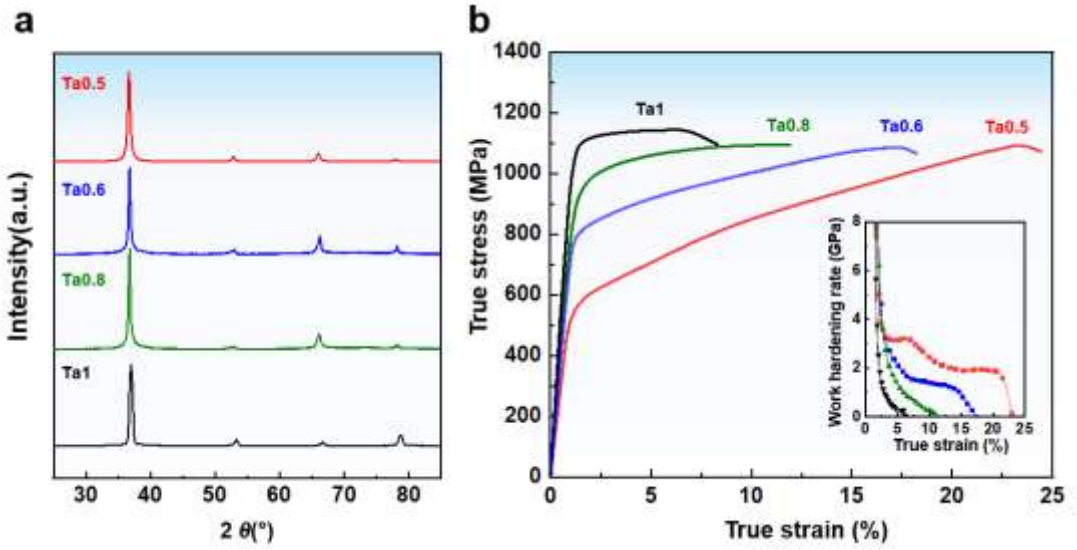

Figure. 1. (a) X-ray diffraction patterns of $TiZrHfTa_x$ (x=1.00, 0.80, 0.60, 0.50) BCC high entropy alloys after annealing at 1173 K for 0.5 hour, (b) the corresponding tensile true stress-strain curves at ambient temperature. Inset presents the corresponding work hardening rate ($d\sigma_T/d\varepsilon_P$) curves against true strain.

Figure. 1b shows tensile true stress-strain curves and their corresponding work hardening rate curves for the $TiZrHfTa_x$ (x=1.00, 0.80, 0.60, 0.50) alloys to aid in distinguishing the evolution of deformation mechanisms with a variation of tantalum

content. The equimolar Ta1 exhibits the highest yield strength and fracture strength of 1057 MPa and 1140 MPa, respectively, but the least ductility of 8.3%. With a decrease of tantalum content, the yield strength of Ta0.8, Ta0.6 and Ta0.5 gradually reduced to 923MPa, 771 MPa and 537 MPa while the fracture stress reached to 1094 MPa, 1084 MPa and 1100 MPa, respectively. Meanwhile, it is worth noting that their plasticity gradually increased to 11.9% (Ta0.8), 18.2% (Ta0.6) and 24.3% (Ta0.5), respectively, implying that their mechanical performance was substantially enhanced with a decrease of tantalum content. Note that a gradual decreasing trend of the elastic modulus of Ta1 to Ta0.5 was also observed in Figure. 1b, which indicates that a decrease of tantalum content may affect the lattice stability of the BCC phase as analogous to that of other metastable BCC high entropy alloys[6].

Illustrated by the inset in Figure. 1b, distinctive work hardening response of the BCC high entropy alloys can be seen with different tantalum concentrations. The work hardening rate curve of Ta1 exhibits a monotonical decrease after yielding which indicates a dislocation-slip-dominated deformation mechanism and agrees well with its high BCC phase stability[23]. Similarly, the work hardening rate curve of Ta0.8 also exhibits a monotonical decrease, but the decreasing trend was greatly alleviated which infers that additional deformation mechanism may take effect. On the contrary, after an initial decrease, Ta0.6 exhibits a plateau with work hardening rate stabilized at ~1.6 GPa in the strain range of 6% to 14% until plastic instability. In Ta0.5, slight rebound of work hardening rate to 3.2 GPa was observed after the initial drop, followed by a gradual decrease between 7% and 15% strain and then maintained at ~2 GPa until the occurrence of plastic instability at ~22% strain. The enhanced work hardening capability in Ta0.6 and Ta0.5 can be ascribed to the activation of additional deformation mechanisms (i.e., deformation induced martensite and deformation twins)[24–26], and details regarding the underlying deformation mechanisms were investigated in following sections.

3.2. Deformation microstructure

To unravel the underlying deformation mechanisms for the enhanced mechanical performance of Ta0.8, Ta0.6 and Ta0.5 alloys, the deformed samples of the three compositions with 8% strain were characterized by electron backscatter diffraction and transmission electron microscopy. Figure. 2a and b show that, besides wide deformation induced α'' martensite plates (around 3 to 5 μm), deformation induced twinning was observed in Ta0.8 (Figure. 2b). The misorientation angle-axis pair across the interface superimposed by yellow lines in Figure. 2b was measured as $<110>_{BCC}51.5°$ which corresponds to the classical $\{332\}<11\bar{3}>_{BCC}$ twinning[27]. Additionally, as shown in Figure. 2b, although most deformation bands are only composed of $\{332\}<11\bar{3}>_{BCC}$ twin, some deformation bands are composed of $\{332\}<11\bar{3}>_{BCC}$ twin that accompanied by adjacent parallel α'' martensite. This phenomenon is generally led by the special origin of the $\{332\}<11\bar{3}>_{BCC}$ twinning in metastable BCC alloys due to the activation of an α'' martensite assisted mechanism[28]. Figure. 2c shows the microstructure of 8% strained Ta0.6. All deformation bands were indexed as α'' martensites which exhibit a specific zig-zag arrangement. Figure. 2d presents that the misorientation angle-axis pair between the V-shaped α'' martensites was measured as $<110>_{\alpha''}80.6°$, which corresponds to a $\{111\}_{\alpha''}$ type I twinning mode that is generally accepted as a transformation twinning mode in shape memory titanium alloys[21]. The transformation twinning is generated to overcome the volume change that caused by the phase transformation[29], which is consistent with the enhanced phase transformation potency in the Ta0.6 alloy, as visualized in Figure. 2c. The deformation microstructure of Ta0.5 at 8% strain is also composed of BCC phase and deformation induced α'' martensites, as shown in Figure. 2e. However, Figure. 2f shows that numerous secondary α'' martensites were located within the primary wide α'' martensite where two different misorientation angle-axis pairs were observed in the point-to-point and point-to-origin misorientation profiles acquired along the arrow across the primary α'' and two different α'' bands. The two misorientation relationships were confirmed as $<011>_{\alpha''}83.3°$ and $<011>_{\alpha''}95.3°$,

which corresponds to $\{111\}_{\alpha''}$ type I twinning and $<\bar{2}11>_{\alpha''}$ type II twinning, respectively[21]. It is noted that the $<\bar{2}11>_{\alpha''}$ type II twinning is also known as a transformation twinning mode[21], whose activation may be attributed to the further reduced BCC phase stability in Ta0.5 when in comparison with the Ta0.6, which will be further discussed by twinning analysis in later section.

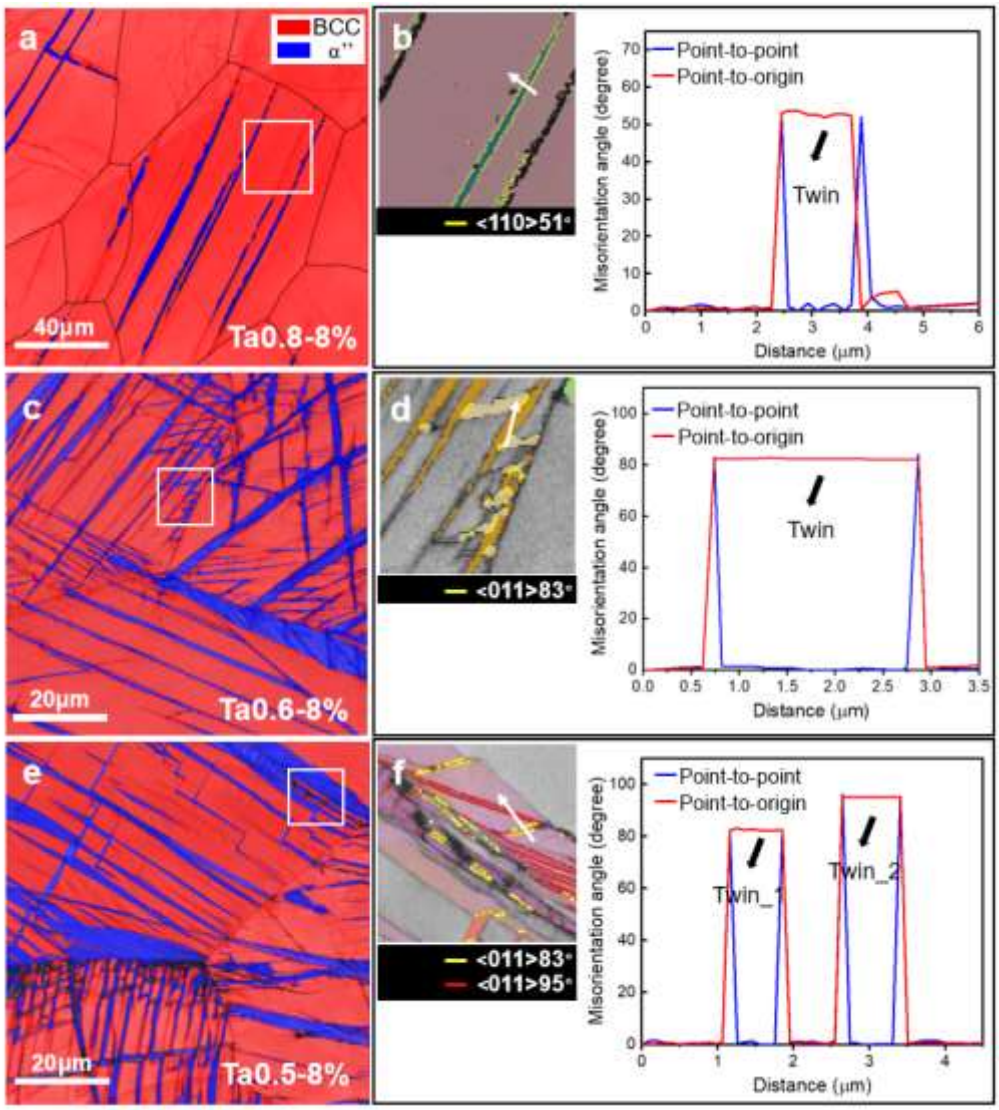

Figure. 2. Electron backscatter diffraction analysis of the deformation bands in deformed samples. (a) Phase map of 8% strained Ta0.8. Red and blue represent BCC and α'' phase, respectively. (b) BCC phase Euler angle map of the boxed region in (a) with misorientation profile taken along the white arrow. (c) Phase map of 8% strained Ta0.6. Red and blue represent BCC and α'' phase, respectively. (d) α'' Euler angle map of the boxed region in (c) with misorientation profile taken along the white arrow. (e) Phase

map of 8% strained Ta0.5. Red and blue represent BCC and α'' phase, respectively. (f) α'' Euler angle map of the boxed region in (e) with misorientation profile taken along the white arrow.

Due to the limited resolution of the electron backscatter diffraction, transmission electron microscopy was employed to further investigate the deformation microstructure of Ta0.8, Ta0.6 and Ta0.5 from nanoscale to atomic scale. In Figure. 3a, thin lamellae within and next to a wide deformation band (~500nm) were observed in 8% deformed Ta0.8. The corresponding selected area diffraction patterns in Figure. 3b determined that the observed feature consists of deformation induced α'' martensites and $\{332\}<11\bar{3}>_{BCC}$ twinning. The dark-filed images in Figure. 3c and d clearly show that the wide deformation band is the $\{332\}<11\bar{3}>_{BCC}$ twinning while the thin lamellae are deformation induced α'' martensites, which corroborates the electron backscatter diffraction result observed in Figure. 2a and may have contribute to refining the microstructure and strengthing the alloy during deformation. Similar α''/$\{332\}<11\bar{3}>_{BCC}$ twin interface has been observed in conventional BCC titanium alloys[28], whose origin has been correlated to an α'' assisted nucleation mechanism in which $\{332\}<11\bar{3}>_{BCC}$ twins nucleate within the progressively formed α'' martensite during deformation.

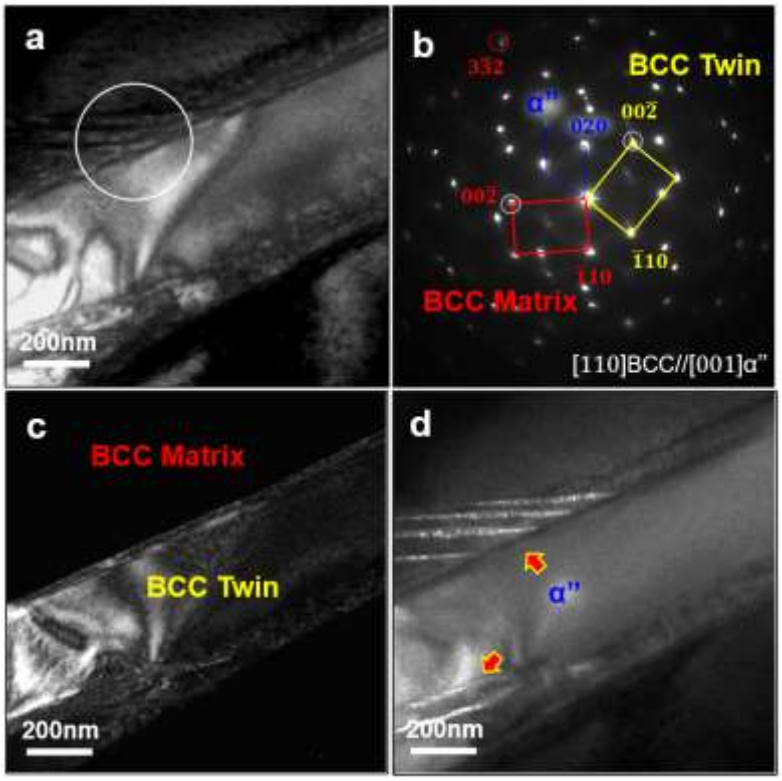

Figure. 3. Microstructures of 8% strained Ta0.8. (a) Bright-field transmission electron microscopy image showing a wide deformation band and several micro bands. (b) Selected area diffraction patterns of the deformation bands marked by white circle in (a). Diffraction spots corresponding to the BCC matrix, BCC twin and α'' martensite are highlighted with red, yellow and blue lines respectively. (c, d) Transmission electron microscopy dark-field images of the BCC twin and α'' martensite taken with circled diffraction spots in (b).

In the 8% strained Ta0.6 sample, complex deformation bands were observed within the BCC matrix (Figure. 4a), while corresponding selected area diffraction patterns reveal that these deformation bands consist of deformation induced α'' martensite and $\{111\}_{\alpha''}$ type I martensitic twinning. Figure. 4b and Figure. 4c present the dark field images of the α'' matrix and $\{111\}_{\alpha''}$ type I twin using the diffraction vector $g=(110)_{\alpha''}$, where a ribbonlike structure (highlighted by red arrows) was observed in the α'' bands and identified as antiphase boundary (APB)-like stacking fault which is accepted as a characteristic feature in α''[30]. Note that APB-like structure has been widely observed in metastable BCC titanium alloys, which is a

consequence of the martensitic transformation and is neither the APB generated by order-disorder transition nor a deformation product[30].

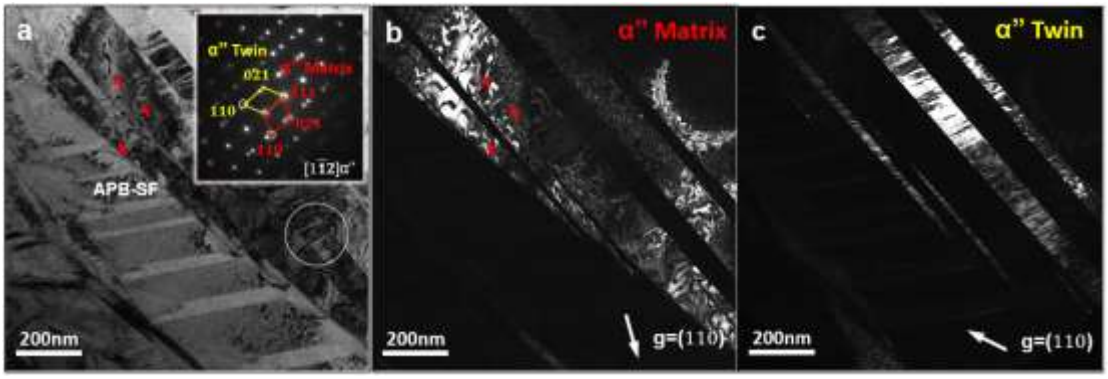

Figure. 4. Martensite deformation products observed in 8% strained Ta0.6. (a) Bright-field transmission electron microscopy image showing the pronounced formation of nanoscale deformation bands. Inset is the indexed selected area diffraction patterns of the deformation bands marked by white circle. The matrix and twinned α'' diffraction spots are highlighted with red and yellow lines, respectively. (b, c) Dark-field images of the α'' matrix and α'' twinning in (a) acquired with diffraction vector $g=(110)_{\alpha''}$.

In the same sample of Figure. 4, as shown in Figure. 5a, a triangular α'' martensitic morphology was visualized. From corresponding selected area diffraction patterns shown in Figure. 5b, this feature consists of three α'' variants (V1-V3) where the orientation relationships between them: V1-V2, V2-V3 and V3-V1 were all identified as $\{111\}_{\alpha''}$ type I twinning. The schematic representation in Figure. 5b summarized the orientation relationship between V1, V2 and V3, and $\sim\{755\}_{BCC}$ was identified as the habit plane of these martensites. Figure. 5c-e show the dark-filed images of V1, V2 and V3, respectively. In Figure. 5c, a thin lath of martensite was highlighted with red arrows and indexed as V1. The thin lath of V1 reaches the boundaries of V2 and V3 where a three-fold $\{111\}_{\alpha''}$ type I twinning is observed. The high-resolution transmission electron microscopy image and corresponding fast Fourier transform image (Figure. 5f) of the triple junction area (marked by the red square in Figure. 5e) established the three-fold twinning relationship between V2, V3 and the thin lath of V1. To the best of our knowledge, this is the first time that a three-fold martensitic twinning feature is captured in BCC high entropy alloys. Similar triangular α'' martensitic feature has been reported in Ti-Nb based metastable shape memory alloys and accepted as a special martensitic

morphology to accommodate the transformation strain[31] which is in agreement with the increased phase transformation potency in the current Ta0.6 alloy. Meanwhile, among V1-V3, twinning terrace (twinning dislocation) was observed along the $\{111\}_{\alpha''V1\&V3}$ and $\{111\}_{\alpha''V1\&V2}$ twinning boundaries, which contributes to the strain minimization during the martensitic transformation process[31].

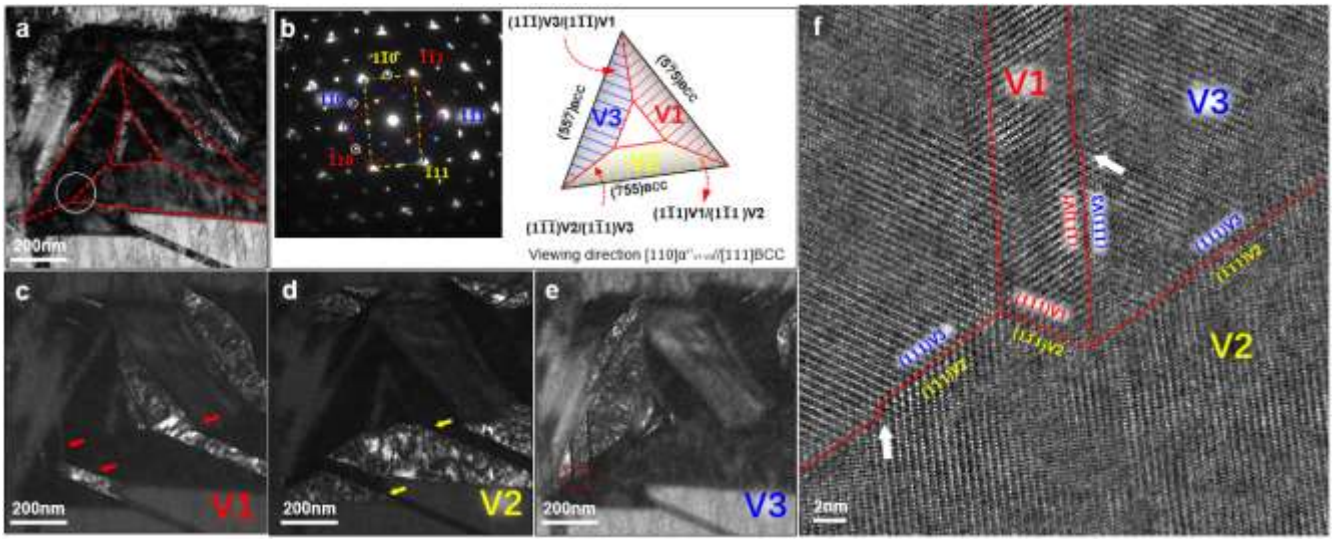

Figure. 5. Triangular morphology of α'' variants observed in 8% strained Ta0.6. (a) Bright-field transmission electron microscopy image showing the triangular shaped α'' variants (highlighted by the dashed red lines). (b) Indexed selected area diffraction patterns taken along the $[110]_{\alpha''}$ zone axis presenting the formation of three martensite variants, V1-V3 (highlighted with red, yellow and blue, respectively); the schematic showing the distribution and orientation relationships between V1, V2 and V3. (c-e) dark field images of V1-V3. (f) transmission electron microscopy image and fast Fourier transform of the red boxed conjunction area (V1-V3) in (e).

In 8% strained Ta0.5, with further reduced BCC stability, extensively activated thin martensites with ~90 nm in thickness were observed within the primary wide α'' martensite (Figure. 6a). Corresponding selected area diffraction patterns acquired along the $[1\bar{1}2]_{\alpha''}$ zone axis in Figure. 6b reveals that the α'' matrix and the deformation bands are related through a special $\{351\}_{\alpha''}$ twinning system. According to the observation on martensitic twinning systems in electron backscatter diffraction result of Figure. 2f, this $\{351\}_{\alpha''}$ twinning is identified as a twinning mode belonging to the $<\bar{2}11>_{\alpha''}$ type II transformation twinning system. Transmission electron microscopy dark-field

images in Figure. 6c and d show the distribution of matrix α'' and the twinned α'', respectively. Figure. 6e displays the high-resolution transmission electron microscopy image of the interface between the α'' matrix and α'' twin. The result further confirms the orientation relationship between α'' matrix and α'' twin which belongs to the $<\bar{2}11>_{\alpha''}$ type II twinning, as the twinned α'' exhibits mirror symmetry across the $(351)_{\alpha''}$ plane with the matrix. It is worth noting that the lattice becomes blurry against the twinning boundary, which could be a result of complex accommodation process caused by twinning dislocations[31]. For type II martensitic twinning modes (e.g., $\{111\}_{B19'}$ of type II $<011>_{B19'}$ twinning in TiNi alloy[32]), the Miller indices of the twinning plane always remain as irrational and the real lattice arrangement of such irrational twinning boundary is composed of continuous rational twinning boundary segments and twinning terrace (twinning dislocations)[33]. Therefore, by following conventional notations which denote the near rational twinning plane of type II twinning system with quotation marks[34,35], the observed type II twinning mode is denoted as ''$\{351\}$''$<\bar{2}11>_{\alpha''}$ type II twinning.

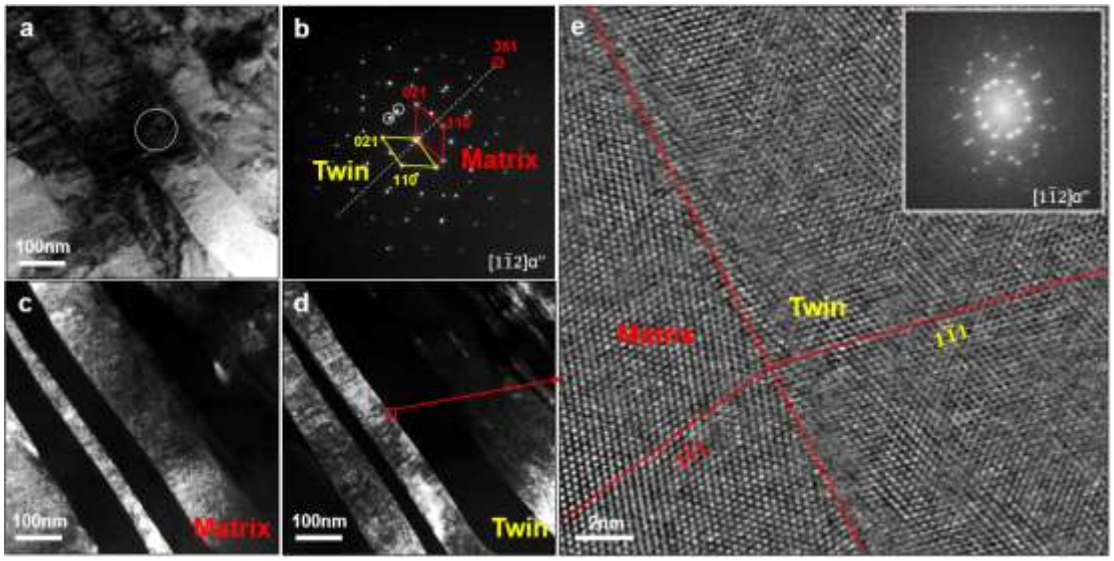

Figure. 6. Martensite deformation products of 8% deformed Ta0.5. (a) Bright-field transmission electron microscopy image of the complex deformation bands. (b) Selected area diffraction patterns of the deformation bands marked by white circle on $[1\text{-}12]_{\alpha''}$ zone axis. The α'' matrix, twinned α'' diffraction spots are highlighted with red and yellow lines respectively. (c, d) Transmission electron microscopy dark-field images of α'' matrix and twinned α'' variant using the diffraction spot indicated in (b). (e)

High-resolution transmission electron microscopy image of the framed area in (d). Inset shows the corresponding fast Fourier transform image of the twinning structure.

The martensite deformation products in Ta0.5 adapted into a more complex structure in comparison with Ta0.6. As shown in Figure. 7a, complex interacted α'' martensites were observed within the parent BCC grain in 8% strained Ta0.5. From the selected area diffraction patterns acquired from the conjunction area of martensites in Figure. 7a, this feature can be primarily identified as a same type of the three-fold $\{111\}_{\alpha''}$ type I twinning as that captured in Figure. 5. However, the three-fold twinning structure in Figure. 7 exhibits a different morphology compared with the triangular one in Ta0.6. Numerous thin lamellae (~20nm) of primary (V2) and secondary (V3) twinned martensites were observed within the primary broad (~240nm) martensite (V1), which dramatically subdivided the coarse martensite microstructure, thereby greatly strengthening the alloy during deformation.

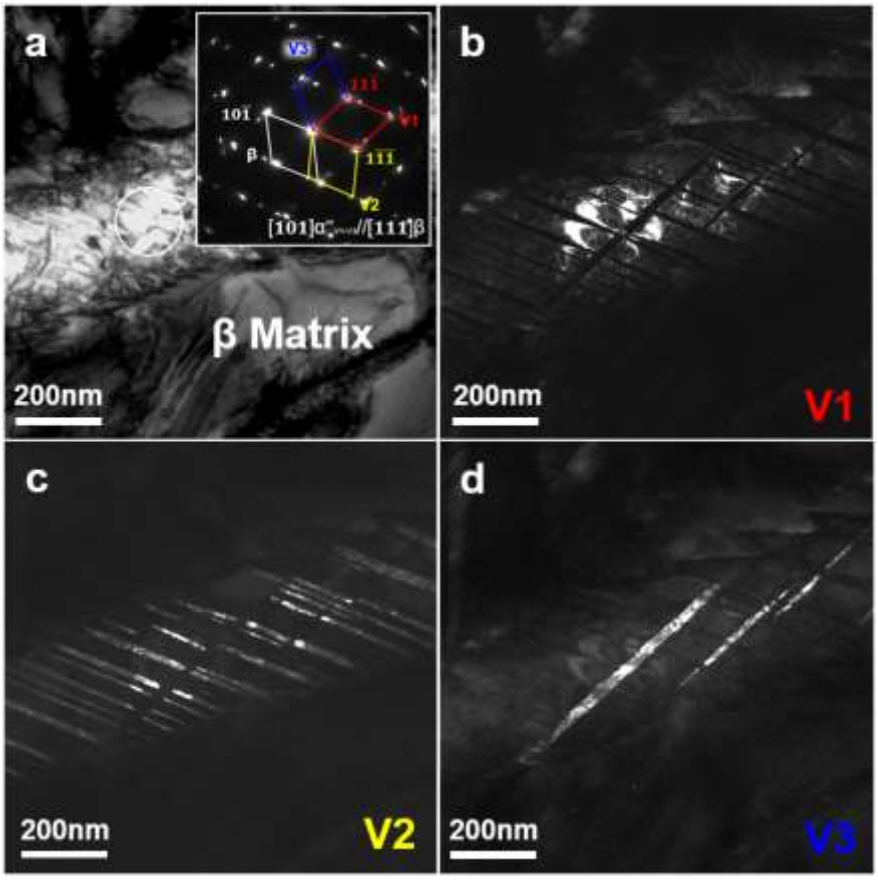

Figure. 7. Martensite deformation bands observed in 8% deformed Ta0.5. (a) Bright-field transmission electron microscopy image of the complex deformation bands. Inset show selected area diffraction

patterns of the deformation bands marked by white circle. The BCC matrix and three α'' variants V1-V3 diffraction spots are highlighted with white, red, yellow, blue lines, respectively. (b-d) Transmission electron microscopy dark-field images of the V1, V2 and V3 variants, respectively.

3.3. Effects of Tantalum content on the deformation behaviour and deformation mechanism selection of $TiZrHfTa_x$ high entropy alloys

It is evident that in the current $TiZrHfTa_x$ (x=1.0, 0.8, 0.6, 0.5) refractory high entropy alloys, representative mechanical properties such as yield strength, work hardening performance and plasticity exhibit obvious dependence on tantalum concentration, as shown in Figure. 1. The gradually reduced tantalum addition from Ta1 to Ta0.5, not only results in the decreased stability of the BCC structure but also a decline on the solid solution strengthening effect as analogous to that of other high entropy alloys[36,37]. Accordingly, the decrease of yield strength with a reduction of tantalum content can be attributed to the reduced solid solution effect and a reduction of critical stress for the activation of specific deformation products, i.e., BCC twinning, deformation induced α'' martensite and martensitic twinning, as less tantalum was added. Moreover, the characterization results of deformed microstructure confirm that the gradual reduction of tantalum content can sequentially trigger the activation of BCC twinning, deformation induced BCC to α'' phase transformation, reorientation of α'' (transformation twinning) and extensively activated α'' transformation twins in Ta0.8, Ta0.6 and Ta0.5 alloys, respectively. Therefore, a decrease of BCC phase stability leads to distinct deformation behavior in these high entropy alloys, as discussed in the following.

During deformation, as expected, with the highest phase stability, Ta1 exhibited the highest yield strength. The monotonous decrease of work hardening rate is thusly attributed to the dislocation-slip-dominated deformation mechanism which is identical to that of the equimolar refractory BCC high entropy alloys with high BCC phase stability[38–40]. With reduced tantalum content, Ta0.8 exhibits improved work hardening capability and uniform strain when compared with the equal-molar Ta1 composition. It is known that in BCC titanium alloys, the reduction of BCC phase

stability will lead to a decrease in the shear modulus $c'((c_{11}-c_{12})/2)$ in BCC structure which causes lattice instability along $\{011\}<0\bar{1}1>_{BCC}$ and further triggers the martensitic phase transformation during fast cooling or continuous loading[41]. This is evident in Ta0.8 where deformation induced α'' martensites were captured by electron backscatter diffraction (Figure. 2a). Meanwhile, benefits from the reduced BCC phase stability, another deformation product, the $\{332\}<11\bar{3}>_{BCC}$ twinning were captured in deformed Ta0.8 (Figure. 2b). Different from the $\{112\}<11\bar{1}>_{BCC}$ deformation twinning which is believed to be formed through successive glide of partial dislocations along $\{112\}_{BCC}$ crystallographic planes and usually observed in BCC metals with high structural stability[42], the $\{332\}<11\bar{3}>_{BCC}$ twinning is more frequently observed in alloys with lower BCC phase stability, and accepted as originating from an α'' assisted mechanism[28,43]. This can be visualized in Figure. 3 where deformation induced α'' martensites is observed adjacent to and within the $\{332\}<11\bar{3}>_{BCC}$ twinning. These twinning and phase boundaries provide effective obstacles for dislocation motion and therefore postpone the plastic instability to higher strains. However, the relatively high tantalum concentration in Ta0.8 leads to high critical stress for the activation of deformation products like deformation induced twinning and deformation induced martensites[22,44], which greatly limits the extent of martensite transformation and twinning. Consequently, the volume fraction of α'' in Ta0.8 is only 5.35%, thus detaining its work hardening capacity at a rather lower level. Consequently, the strengthening effect of deformation twinning and martensites (TWIP and TRIP) are suppressed in Ta0.8, thus leading to higher yield strength but lower uniform elongation when compared with Ta0.6 and Ta0.5.

Table 1

Volume fraction and average thickness of the α'' martensite in 8% strained Ta0.8, Ta0.6 and Ta0.5 alloys.

Alloys	Volume fraction of α''	Average thickness of α'' plate	Volume fraction of martensitic twins
Ta0.8	5.35%	3.16μm	—
Ta0.6	19.92%	1.87μm	7.17%

Ta0.5	45.07%	0.76μm	21.67%

In Ta0.6, the further decrease of tantalum content destabilized the BCC structure and accordingly, the yield strength was reduced to 771MPa. Meanwhile, the further decreased stability of BCC structure lowered the critical stress for the activation of martensitic transformation, resulting in its prior activation in comparison with that in Ta0.8. As shown in Table. 1, at 8% strain, the volume fraction of the martensite was increased from 5.35% of Ta0.8 to 19.92% of Ta0.6.

Owing to the special lattice correspondence between BCC structure and orthorhombic structure of α'' phase, six possible lattice correspondences martensitic α'' variants in one BCC parent grain can be expected, as listed in Table. 2. During deformation induced martensitic transformation, to accommodate the deformation strain, one martensitic α'' variant tends to reorientate into another martensitic α'' variant without introducing macroscopic shape change by twinning[21,45], which is known as transformation twinning. In the deformed Ta0.6, various martensitic deformation products were discovered within this accommodation morphology. For example, the $\{111\}_{\alpha''}$ type I transformation twinning was captured with characteristic APB-like stacking fault of α'' martensite, as shown in Figure. 4. Meanwhile, mimic to the Ti-based shape memory alloy[31], a triangular martensitic morphology formed by three-fold $\{111\}_{\alpha''}$ type I twinning was observed (Figure. 5) which indicates the obvious reorientation behavior of martensite in Ta0.6. In accordance with that in BCC titanium alloys, transformation twinning and the corresponding reorientation of martensite variants are effective approaches to accommodating deformation strain in metastable BCC high entropy alloys[12]. Moreover, the generation of extensive transformation twins in Ta0.6 greatly refined the primary coarse martensite to 1.87μm (average thickness), much smaller than that of Ta0.8 (3.16μm). Therefore, ascribed to the cooperation of deformation-induced martensite and martensitic transformation twinning, after yielding, the work hardening rate of Ta0.6 was maintained at a higher

level (~1.6 GPa) due to the dynamic Hall–Petch effect, which postpones the occurrence of plastic instability, yielding a total elongation of 18.2% in Ta0.6.

Table 2

The six α'' lattice correspondence variants of parent BCC

	$[1\ 0\ 0]_{\alpha''}$	$[0\ 1\ 0]_{\alpha''}$	$[0\ 0\ 1]_{\alpha''}$
V1	$[1\ 0\ 0]_{BCC}$	$[0\ 1\ 1]_{BCC}$	$[0\ \bar{1}\ 1]_{BCC}$
V2	$[1\ 0\ 0]_{BCC}$	$[0\ \bar{1}\ 1]_{BCC}$	$[0\ \bar{1}\ \bar{1}]_{BCC}$
V3	$[0\ 1\ 0]_{BCC}$	$[1\ 0\ 1]_{BCC}$	$[1\ 0\ \bar{1}]_{BCC}$
V4	$[0\ 1\ 0]_{BCC}$	$[1\ 0\ \bar{1}]_{BCC}$	$[\bar{1}\ 0\ \bar{1}]_{BCC}$
V5	$[0\ 0\ 1]_{BCC}$	$[1\ 1\ 0]_{BCC}$	$[\bar{1}\ 1\ 0]_{BCC}$
V6	$[0\ 0\ 1]_{BCC}$	$[\bar{1}\ 1\ 0]_{BCC}$	$[\bar{1}\ \bar{1}\ 0]_{BCC}$

Finally, with the least tantalum content, Ta0.5 possesses the lowest BCC phase stability, resulting in a low yield strength of 537 MPa which is 520 MPa smaller than that in Ta1. Accordingly, the Ta0.5 exhibits the lowest elastic modulus among all the tested compositions, which indicates that the reduction of BCC phase stability decreased the shear modulus $c'((c_{11}-c_{12})/2)$ in the stable BCC structure[43], causing instability of the BCC lattice and resulting in the lowered elastic modulus. As a result, Ta0.5 possesses the most promoted martensite transformation potency as shown in Figure. 2e and Table. 2 and thus the work hardening capability of Ta0.5 is greatly enhanced in comparison with other compositions (even with the Ta0.6). As shown in Figure. 1b, the work hardening rate of this alloy peaked at 3.2 GPa around 7% strain and sustained as high as 2-3 GPa until fracture, which enabled an enhanced fracture strength of 1100 MPa and total elongation of 24.3%. Besides, the comprehensively improved mechanical performance of Ta0.5 could be attributed to the extensive activation of twinning in the deformation induced α'' martensite. The volume fraction of the α'' climbs to 45.07% in Ta0.5, which promotes the activation of transformation twinning and increases the volume fraction of the martensitic twins to 21.67%, much higher than that of Ta0.6 (7.17%). In addition to the martensitic

deformation products observed in Ta0.6, a ‘‘$\{351\}$’’$<\bar{2}11>_{\alpha''}$ type II transformation twinning was activated in Ta0.5, as shown in Figure. 6. Moreover, the three-fold $\{111\}_{\alpha''}$ type I twinning was also captured in Ta0.5, however, instead of sharing a triangular morphology with that in Ta0.6 (Figure. 5), numerous thin laths of two $\{111\}_{\alpha''}$ type I twinned martensitic variants were observed within the primary wide martensite (Figure. 7).

To unravel the underlying mechanisms responsible for the extensive occurrence of the thin type I and type II transformation twinning in Ta0.5, here, the twinning elements of the $\{111\}_{\alpha''}$ type I and $<\bar{2}11>_{\alpha''}$ type II twinning were calculated via the deformation twinning theory[46] and listed in Table. 3. The lattice parameters for Ta0.5 were measured to be $a_{\alpha''}$ = 3.221Å, $b_{\alpha''}$ = 5.151Å, and $c_{\alpha''}$ = 4.921Å, while those of Ta0.6 were $a_{\alpha''}$ = 3.245Å, $b_{\alpha''}$ = 5.121Å, and $c_{\alpha''}$ = 4.913Å. It is noted that the $\{111\}_{\alpha''}$ type I twinning is conjugate of $<\bar{2}11>_{\alpha''}$ type II twinning which is identical to that proposed by Inamura co-workers[21] in BCC titanium alloys. The twinning elements of the $\{111\}_{\alpha''}$ type I and $<\bar{2}11>_{\alpha''}$ type II transformation twinning are highly dependent on the lattice parameters of the α’’ martensite which are associated with the concentration of tantalum content in TiZrHfTa. The magnitude of the twinning shear vector of Ta0.5 is smaller than that of Ta0.6 (Table. 3), thus lower energy (smaller critical stress) is required in Ta0.5 for activating such transformation twins. Consequently, owing to the reduced phase stability, the deformed microstructure in Ta0.5 becomes more complex in which the dense lamellar martensites and martensitic transformation twins keep refining the structure while accommodating the deformation strain, thusly contributing to the high work hardening capability and synergetic high ductility and ultimate tensile strength of Ta0.5.

Table. 3

Twinning elements of $\{111\}_{\alpha''}$ type I and $<\bar{2}11>_{\alpha''}$ type II twins calculated from the lattice parameters of the Ta0.5 and Ta0.6 alloys.

Ta0.5	$\boldsymbol{K_1}$	$\boldsymbol{K_2}$	$\boldsymbol{\eta_1}$	$\boldsymbol{\eta_2}$	s

$\{111\}_{\alpha''}$ Type I	{1 1 1}	{1, $\overline{4.3}$, 2.3}	<1, $\overline{2.1}$, 1.1>	<211>	0.1366
$<\bar{2}11>_{\alpha''}$ Type II	{1, $\overline{4.3}$, 2.3}	{1 1 1}	<211>	<1, $\overline{2.1}$, 1.1>	0.1366
Ta0.6	K_1	K_2	η_1	η_2	s
$\{111\}_{\alpha''}$ Type I	{1 1 1}	{1, $\overline{3.5}$, 1.5}	<1.4, $\overline{2.4}$, 1>	<211>	0.1508
$<\bar{2}11>_{\alpha''}$ Type II	{1, $\overline{3.5}$, 1.5}	{1 1 1}	<211>	<1.4, $\overline{2.4}$, 1>	0.1508

Present results provide essential evidence that the selection of deformation mechanisms in refractory elements-based metastable BCC high entropy alloys is highly dependent on the content of BCC stabilizer, herein tantalum. To quantify the effect of BCC stabilizer addition on tuning phase stability and further on deformation mechanism selection in BCC high entropy alloys, mimic its conventional IVB element counterparts, i.e., Titanium alloys, two electronic parameters, Bo and Md were employed to evaluate the chemical stability of the BCC phase in current BCC high entropy alloys. Initially proposed by Kuroda co-workers[18] and later by Abdel-Hady co-workers[19], the Bo-Md map was applied as an efficient guidance to measure the BCC phase stability and further to predict possible deformation mechanisms, i.e., dislocation slip, TRIP and TWIP, in BCC titanium alloys (i.e., Ti-9Mo-6W[47] and Ti-7Mo-3Cr[48]). It was confirmed recently that the Bo−Md map is applicable for the development of metastable refractory elements based BCC high entropy alloys[6,11,20,49]. However, due to the multi-component nature of high entropy alloys, the calculated Bo and Md values of most BCC high entropy alloys (e.g., Bo=3.016 and Md=2.749 for TiZrHfTa, Bo=3.045 and Md=2.662 for TiZrHfNbTa) are out of the range (2.8<Bo<2.9 and 2.3<Md<2.6) for conventional Bo-Md map of BCC titanium alloys[18,19], limiting the application of Bo-Md map in guiding new metastable BCC high entropy alloys development. In Figure. 8a, we extended the Bo-Md diagram based on present results with identified deformation mechanisms and the Bo-Md map of BCC titanium alloys[19]. The epitaxial M_s = RT line (M_s: the start temperature of martensitic transformation, and RT: room temperature), slip/twin boundary, twin/α'' martensite boundary, α''/α' boundary and α'/α boundary were strategically extended in Figure. 8

according to the positions of different BCC high entropy alloys. Apparently, an increment of BCC stabilizer's content leads to reduction in Bo but an enhancement in Md which is expected to move the alloys position from α-stable region to BCC stable region in the diagram and sequentially across the α'/α boundary, α''/α' boundary, twin/α'' martensite boundary and slip/twin boundary. This transition trend is consistent with the observed activation sequence of the plastic deformation mechanism from promoted α'' martensitic twinning (Ta0.5), attenuated self-accommodated α'' martensitic structure (Ta0.6), to deformation-induced α'' and $\{332\}_{BCC}$ deformation twinning (Ta0.8) with an increase of BCC phase stability from Ta0.5 to Ta0.8, as shown in Figure. 8b. As for Ta1, with the highest BCC phase stability, dislocation slip becomes the predominant deformation mechanism, akin to that of stable BCC structural alloys[38]. In addition, reported metastable BCC high entropy alloys, such as Ti35Zr27.5Hf27.5Nb5Ta5[11] and TiZrHfTa0.2Nbx(x=0, 0.15, 0.2, 0.25)[10], etc., are located within the martensite region while Ti48.9Zr32Nb12.6Ta6.5[20] is located within the BCC twin region, which corresponds well with their reported deformation mechanisms. Therefore, the extended Bo-Md map could be utilized as an effective reference for the design of new BCC high entropy alloys with expected deformation mechanisms. Meanwhile, it is suggested that the phase stability and thus the deformation mechanisms in BCC high entropy alloys can be effectively tuned by adjusting the content of BCC stabilizer so as to optimize their mechanical properties.

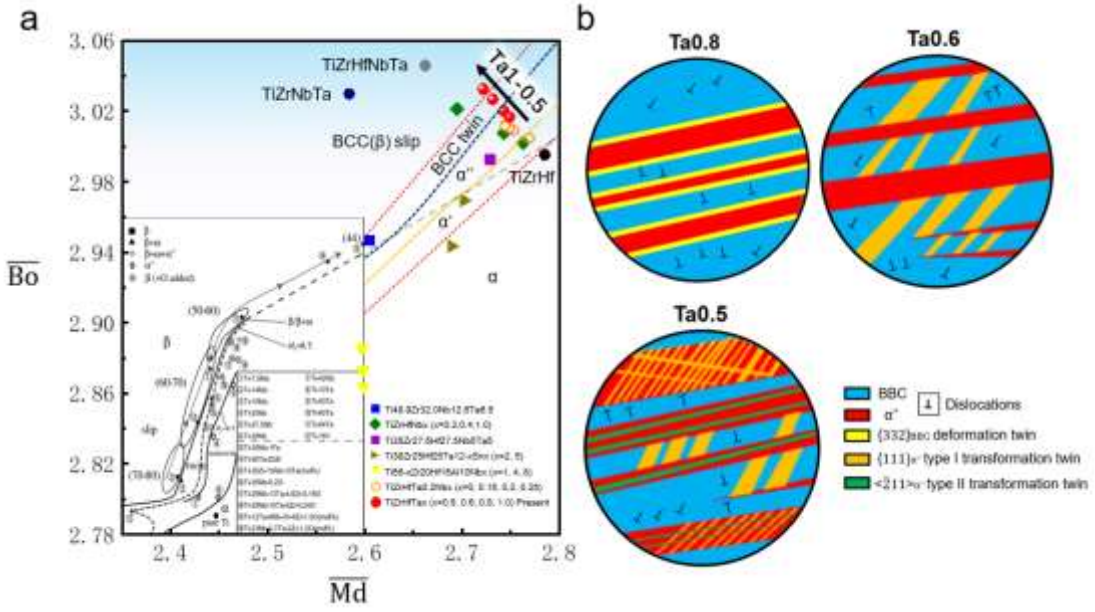

Figure. 8. (a) Extended $\overline{Bo}$-$\overline{Md}$ diagram with values of current $TiZrHfTa_{x\ (x=0.5,\ 0.6,\ 0.8,\ 1.0)}$ and several reported BCC high entropy alloys[6,8,10,11,20,50]. (b) Illustration of deformation mechanisms evolution from Ta0.8 to Ta0.5.

4 Conclusions

In summary, the effects of tantalum on TiZrHfTax (x=1.00, 0.80, 0.60, 0.50) BCC high entropy alloys' deformation behavior and deformation mechanisms were systematically investigated in the present work. On the basis of experimental results and discussion, the following conclusions can be drawn:

(1) In the thermomechanical treated TiZrHfTax (x=1.00, 0.80, 0.60, 0.50) BCC high entropy alloys, via adjusting the amount of BCC stabilizer, tantalum, from Ta1 to Ta0.5, the BCC phase stability and the yield strength were gradually decreased, whilst the work hardening capability and ductility were greatly enhanced.

(2) Electron backscatter diffraction and transmission electron microscopy results of deformed Ta0.8, Ta0.6 and Ta0.5 samples present convincing evidence for the effect of tantalum content on the activation of specific deformation mechanisms in current BCC high entropy alloys. With decreasing content of tantalum,

$\{332\}\langle 11\bar{3}\rangle_{BCC}$ mechanical twinning (in Ta0.8), deformation induced α'' martensite (in Ta0.8, Ta0.6 and Ta0.5) and $\{111\}_{\alpha''}$ type I twinning (Ta0.6 and Ta0.5) were sequentially activated. A specific $\langle\bar{2}11\rangle_{\alpha''}$ type II twinning was identified in Ta0.5, and further selected area diffraction patterns and high-resolution transmission electron microscopy analysis identified that the twinning plane of the observed $\langle\bar{2}11\rangle_{\alpha''}$ type II twinning is a near rational ''$\{351\}$''$_{\alpha''}$ plane.

(3) The strengthening effects of multiple deformation mechanisms, i.e., $\{332\}\langle 11\bar{3}\rangle_{BCC}$ mechanical twinning, deformation induced α'' martensites and martensitic twins, were discussed, which determined the distinctive work-hardening behavior among the current $TiZrHfTa_x$. With the lowest tantalum content, Ta0.6 and Ta0.5 possess the best combination of strength and ductility among the current series (1084 MPa and 18.2% for Ta0.6, 1100 MPa and 24.3% for Ta0.5), and the martensitic twinning is ascribed as their predominant deformation mechanism. The calculation of the magnitude of the martensitic twinning shear for Ta0.5 and Ta0.6 illustrates the obvious dependence of deformation mechanism on the tantalum content. The smaller magnitude of the twinning shear in the Ta0.5 alloy lowers the twinning activation energy in martensite and explains the correspondingly high work hardening capability and complex deformation microstructure, which results in the relatively higher work hardening rate and larger elongation.

(4) The effects of tantalum content on tuning phase stability and deformation mechanisms selection (deformation twinning in BCC phase, deformation induced martensite and martensitic transformation twinning, etc) in refractory BCC high entropy alloys were discussed. And on the basis of present work and reported BCC high entropy alloys, an extended Bo-Md map was pictured which could be utilized to design new BCC high entropy alloys with expected deformation mechanisms and enhanced mechanical performance.

Acknowledgements

The authors gratefully acknowledge funding through Shenzhen Science and Technology Innovation Commission (Grant No. KQTD20170328154443162, ZDSYS201703031748354) and support from the Engineering and Physical Sciences Research Council (EPSRC) grants EP/P006566/1 under Manufacture using Advanced Powder Processes (MAPP) and the Henry Royce Institute for Advanced Materials, funded through EPSRC grants EP/R00661X/1, EP/S019367/1, EP/P02470X/1 and EP/P025285/1. DG would like to thank the UKRI for his Future Leaders Fellowship, MR/T019123/1. The authors would also like to acknowledge the technical support from Southern University of Science and Technology Core Research Facilities.

CRediT authorship contribution statement

Yuhe Huang: Conceptualization, Investigation, Writing – original draft. **Junheng Gao**: Conceptualization, Investigation, Writing - review & editing. **Shuize Wang:** Investigation, Writing - review & editing. **Dikai Guan**: Investigation. **Yidong Xu**: Investigation. **Xiaogang Hu**: Investigation. **W.Mark Rainforth:** Supervision, Writing - review & editing. **Qiang Zhu**: Investigation, Writing - review & editing. **Iain Todd**: Conceptualization, Supervision, Writing - review & editing.

References

[1] O.N. Senkov, D.B. Miracle, K.J. Chaput, J.P. Couzinie, Development and exploration of refractory high entropy alloys - A review, J. Mater. Res. (2018). doi:10.1557/jmr.2018.153.

[2] O.N. Senkov, G.B. Wilks, J.M. Scott, D.B. Miracle, Mechanical properties of Nb25Mo25Ta25W25 and V20Nb20Mo20Ta20W20 refractory high entropy alloys, Intermetallics. (2011). doi:10.1016/j.intermet.2011.01.004.

[3] C.C. Juan, M.H. Tsai, C.W. Tsai, C.M. Lin, W.R. Wang, C.C. Yang, S.K. Chen, S.J. Lin, J.W. Yeh, Enhanced mechanical properties of HfMoTaTiZr and HfMoNbTaTiZr refractory high-entropy alloys, Intermetallics. (2015). doi:10.1016/j.intermet.2015.03.013.

[4] J. Chen, X. Zhou, W. Wang, B. Liu, Y. Lv, W. Yang, D. Xu, Y. Liu, A review on fundamental of high entropy alloys with promising high–temperature properties, J. Alloys Compd. (2018). doi:10.1016/j.jallcom.2018.05.067.

[5] H. Huang, Y. Wu, J. He, H. Wang, X. Liu, K. An, W. Wu, Z. Lu, Phase-Transformation Ductilization of Brittle High-Entropy Alloys via Metastability Engineering, Adv. Mater. (2017). doi:10.1002/adma.201701678.

[6] X. Wen, Y. Wu, H. Huang, S. Jiang, H. Wang, X. Liu, Y. Zhang, X. Wang, Z. Lu, Effects of Nb on deformation-induced transformation and mechanical properties of HfNbxTa0.2TiZr high entropy alloys, Mater. Sci. Eng. A. Struct. Mater. 805 (2021) 140798. doi:10.1016/j.msea.2021.140798.

[7] L. Rogal, U.D. Wdowik, M. Szczerba, N. Yurchenko, T. Czeppe, P. Bobrowski, Deformation induced twinning in hcp/bcc Al10Hf25Nb5Sc10Ti25Zr25 high entropy alloy – microstructure and mechanical properties, Mater. Sci. Eng. A. Struct. Mater. 802 (2021). doi:10.1016/j.msea.2020.140449.

[8] R.R. Eleti, M. Klimova, M. Tikhonovsky, N. Stepanov, S. Zherebtsov, Exceptionally high strain-hardening and ductility due to transformation induced plasticity effect in Ti-rich high-entropy alloys, Sci. Rep. (2020). doi:10.1038/s41598-020-70298-2.

[9] Y. Jung, K. Lee, S.J. Hong, J.K. Lee, J. Han, K.B. Kim, P.K. Liaw, C. Lee, G. Song, Investigation of phase-transformation path in TiZrHf(VNbTa)x refractory high-entropy alloys and its effect on mechanical property, J. Alloys Compd. 886 (2021). doi:10.1016/j.jallcom.2021.161187.

[10] L. Zhang, H. Fu, S. Ge, Z. Zhu, H. Li, H. Zhang, A. Wang, H. Zhang, Phase transformations in body-centered cubic NbxHfZrTi high-entropy alloys, Mater. Charact. 142 (2018) 443–448. doi:10.1016/j.matchar.2018.06.012.

[11] L. Lilensten, J.P. Couzinié, J. Bourgon, L. Perrière, G. Dirras, F. Prima, I. Guillot, Design and tensile properties of a bcc Ti-rich high-entropy alloy with transformation-induced plasticity, Mater. Res. Lett. (2017). doi:10.1080/21663831.2016.1221861.

[12] L. Wang, C. Fu, Y. Wu, R. Li, Y. Wang, X. Hui, Ductile Ti-rich high-entropy alloy controlled by stress induced martensitic transformation and mechanical twinning, Mater. Sci. Eng. A. (2019). doi:10.1016/j.msea.2019.138147.

[13] L. Wang, T. Cao, X. Liu, B. Wang, K. Jin, Y. Liang, L. Wang, F. Wang, Y. Ren, J. Liang, Y. Xue, A novel stress-induced martensitic transformation in a single-phase refractory high-entropy alloy, Scr. Mater. 189 (2020) 129–134. doi:10.1016/j.scriptamat.2020.08.013.

[14] Z. Li, C.C. Tasan, H. Springer, B. Gault, D. Raabe, Interstitial atoms enable joint twinning and transformation induced plasticity in strong and ductile high-entropy alloys, Sci. Rep. (2017). doi:10.1038/srep40704.

[15] W. Lu, C.H. Liebscher, G. Dehm, D. Raabe, Z. Li, Bidirectional Transformation Enables Hierarchical Nanolaminate Dual-Phase High-Entropy Alloys, Adv. Mater. (2018). doi:10.1002/adma.201804727.

[16] Y. Deng, C.C. Tasan, K.G. Pradeep, H. Springer, A. Kostka, D. Raabe, Design of a twinning-induced plasticity high entropy alloy, Acta Mater. (2015). doi:10.1016/j.actamat.2015.04.014.

[17] Z. Li, K.G. Pradeep, Y. Deng, D. Raabe, C.C. Tasan, Metastable high-entropy dual-phase alloys overcome the strength-ductility trade-off, Nature. (2016). doi:10.1038/nature17981.

[18] D. Kuroda, M. Niinomi, M. Morinaga, Y. Kato, T. Yashiro, Design and mechanical properties of new β type titanium alloys for implant materials, Mater. Sci. Eng. A. Struct. Mater. 243 (1998) 244–249. doi:10.1016/S0921-5093(97)00808-3.

[19] M. Abdel-Hady, K. Hinoshita, M. Morinaga, General approach to phase stability and elastic properties of β-type Ti-alloys using electronic parameters, Scr. Mater. (2006). doi:10.1016/j.scriptamat.2006.04.022.

[20] X. Zhang, W. Wang, J. Wu, S. Wang, J. Sun, J.Y. Chung, S.J. Pennycook, Deformation twinning in Ti48.9Zr32.0Nb12.6Ta6.5 medium entropy alloy, Mater. Sci. Eng. A. Struct. Mater. 809 (2021) 140931. doi:10.1016/j.msea.2021.140931.

[21] T. Inamura, J.I. Kim, H.Y. Kim, H. Hosoda, K. Wakashima, S. Miyazaki, Composition dependent crystallography of α″-martensite in Ti-Nb-based β-titanium alloy, Philos. Mag. (2007). doi:10.1080/14786430601003874.

[22] M. Ahmed, D. Wexler, G. Casillas, O.M. Ivasishin, E. V. Pereloma, The influence of β phase stability on deformation mode and compressive mechanical properties of Ti-10V-3Fe-3Al alloy, Acta Mater. (2015). doi:10.1016/j.actamat.2014.10.043.

[23] A. Rohatgi, K.S. Vecchio, G.T. Gray, The influence of stacking fault energy on the mechanical behavior of Cu and Cu-al alloys: Deformation twinning, work hardening, and dynamic recovery, Metall. Mater. Trans. A Phys. Metall. Mater. Sci. (2001). doi:10.1007/s11661-001-0109-7.

[24] F. Sun, J.Y. Zhang, M. Marteleur, T. Gloriant, P. Vermaut, D. Laillé, P. Castany, C. Curfs, P.J. Jacques, F. Prima, Investigation of early stage deformation mechanisms in a metastable β titanium alloy showing combined twinning-induced plasticity and

transformation-induced plasticity effects, Acta Mater. (2013). doi:10.1016/j.actamat.2013.07.019.

[25] M. Marteleur, F. Sun, T. Gloriant, P. Vermaut, P.J. Jacques, F. Prima, On the design of new β-metastable titanium alloys with improved work hardening rate thanks to simultaneous TRIP and TWIP effects, Scr. Mater. (2012). doi:10.1016/j.scriptamat.2012.01.049.

[26] T. Yang, Y.L. Zhao, Y. Tong, Z.B. Jiao, J. Wei, J.X. Cai, X.D. Han, D. Chen, A. Hu, J.J. Kai, K. Lu, Y. Liu, C.T. Liu, Multicomponent intermetallic nanoparticles and superb mechanical behaviors of complex alloys, Science (80-.). (2018). doi:10.1126/science.aas8815.

[27] E. Bertrand, P. Castany, I. Péron, T. Gloriant, Twinning system selection in a metastable $β$-titanium alloy by Schmid factor analysis, Scr. Mater. 64 (2011) 1110–1113.

[28] M.J. Lai, C.C. Tasan, D. Raabe, On the mechanism of {332} twinning in metastable β titanium alloys, Acta Mater. (2016). doi:10.1016/j.actamat.2016.03.040.

[29] K. Bhattacharya, others, Microstructure of martensite: why it forms and how it gives rise to the shape-memory effect, Oxford University Press, 2003.

[30] T. Inamura, H. Hosoda, H. Young Kim, S. Miyazaki, Antiphase boundary-like stacking fault in α″-martensite of disordered crystal structure in β-titanium shape memory alloy, Philos. Mag. (2010). doi:10.1080/14786435.2010.489889.

[31] Y.W. Chai, H.Y. Kim, H. Hosoda, S. Miyazaki, Self-accommodation in Ti-Nb shape memory alloys, Acta Mater. (2009). doi:10.1016/j.actamat.2009.04.051.

[32] Z.L. Xie, Y. Liu, HRTEM study of (011) type II twin in NiTi shape memory alloy, Philos. Mag. (2004). doi:10.1080/14786430412331283596.

[33] A.S.K. Mohammed, H. Sehitoglu, Modeling the interface structure of type II twin boundary in B19′ NiTi from an atomistic and topological standpoint, Acta Mater. (2020). doi:10.1016/j.actamat.2019.10.048.

[34] R.W. Cahn, Plastic deformation of alpha-uranium, Acta Metall. 1 (1953) 49,IN1,53-52,IN5,70. doi:10.1016/0001-6160(53)90009-1.

[35] Y. Yang, P. Castany, Y.L. Hao, T. Gloriant, Plastic deformation via hierarchical nano-sized martensitic twinning in the metastable β Ti-24Nb-4Zr-8Sn alloy, Acta Mater. 194 (2020) 27–39. doi:10.1016/j.actamat.2020.04.021.

[36] C.C. Juan, K.K. Tseng, W.L. Hsu, M.H. Tsai, C.W. Tsai, C.M. Lin, S.K. Chen, S.J. Lin, J.W. Yeh, Solution strengthening of ductile refractory HfMoxNbTaTiZr high-entropy alloys, Mater. Lett. (2016). doi:10.1016/j.matlet.2016.03.133.

[37] C. Varvenne, W.A. Curtin, Strengthening of high entropy alloys by dilute solute additions: CoCrFeNiAlx and CoCrFeNiMnAlx alloys, Scr. Mater. 138 (2017) 92–95. doi:https://doi.org/10.1016/j.scriptamat.2017.05.035.

[38] Y.D. Wu, Y.H. Cai, T. Wang, J.J. Si, J. Zhu, Y.D. Wang, X.D. Hui, A refractory Hf 25 Nb 25 Ti 25 Zr 25 high-entropy alloy with excellent structural stability and tensile properties, Mater. Lett. (2014). doi:10.1016/j.matlet.2014.05.134.

[39] F. Wang, G.H. Balbus, S. Xu, Y. Su, J. Shin, P.F. Rottmann, K.E. Knipling, J.C. Stinville, L.H. Mills, O.N. Senkov, I.J. Beyerlein, T.M. Pollock, D.S. Gianola, Multiplicity of dislocation pathways in a refractory multiprincipal element alloy, Science. (2020). doi:10.1126/science.aba3722.

[40] C. Lee, F. Maresca, R. Feng, Y. Chou, T. Ungar, M. Widom, K. An, J.D. Poplawsky, Y.-C. Chou, P.K. Liaw, others, Strength can be controlled by edge dislocations in refractory high-entropy alloys, Nat. Commun. 12 (2021) 1–8.

[41] H.Y. Kim, L. Wei, S. Kobayashi, M. Tahara, S. Miyazaki, Nanodomain structure and its effect on abnormal thermal expansion behavior of a Ti-23Nb-2Zr-0.7Ta-1.2O alloy, Acta Mater. 61 (2013) 4874–4886. doi:10.1016/j.actamat.2013.04.060.

[42] J. Wang, Z. Zeng, C.R. Weinberger, Z. Zhang, T. Zhu, S.X. Mao, In situ atomic-scale observation of twinning-dominated deformation in nanoscale body-centred cubic tungsten, Nat Mater. 14 (2015) 594–600. doi:10.1038/nmat4228.

[43] H. Tobe, H.Y. Kim, T. Inamura, H. Hosoda, S. Miyazaki, Origin of {3 3 2} twinning in metastable β-Ti alloys, Acta Mater. (2014). doi:10.1016/j.actamat.2013.10.048.

[44] T. Grosdidier, Y. Combres, E. Gautier, M.-J. Philippe, Effect of microstructure variations on the formation of deformation-induced martensite and associated tensile properties in a $β$ metastable Ti alloy, Metall. Mater. Trans. A. 31 (2000) 1095–1106.

[45] K. Bhattacharya, Self-accommodation in martensite, Arch. Ration. Mech. Anal. (1992). doi:10.1007/BF00375026.

[46] B.A. Bilby, A.G. Crocker, The Theory of the Crystallography of Deformation Twinning, Proc. R. Soc. A Math. Phys. Eng. Sci. (1965). doi:10.1098/rspa.1965.0216.

[47] F. Sun, J.Y. Zhang, M. Marteleur, C. Brozek, E.F. Rauch, M. Veron, P. Vermaut, P.J. Jacques, F. Prima, A new titanium alloy with a combination of high strength, high strain hardening and improved ductility, Scr. Mater. (2015). doi:10.1016/j.scriptamat.2014.09.005.

[48] J. Gao, Y. Huang, D. Guan, A.J. Knowles, L. Ma, D. Dye, W.M. Rainforth, Deformation mechanisms in a metastable beta titanium twinning induced plasticity alloy with high yield strength and high strain hardening rate, Acta Mater. (2018). doi:10.1016/j.actamat.2018.04.035.

[49] L. Wang, C. Fu, Y. Wu, R. Li, X. Hui, Y. Wang, Superelastic effect in Ti-rich high entropy alloys via stress-induced martensitic transformation, Scr. Mater. (2019). doi:10.1016/j.scriptamat.2018.10.035.

[50] L. Wang, C. Fu, Y. Wu, Q. Wang, X. Hui, Y. Wang, Formation and toughening of metastable phases in TiZrHfAlNb medium entropy alloys, Mater. Sci. Eng. A. 748 (2019) 441–452.